# Journal of
# Materials Chemistry B

Materials for biology and medicine

ROYAL SOCIETY
OF CHEMISTRY
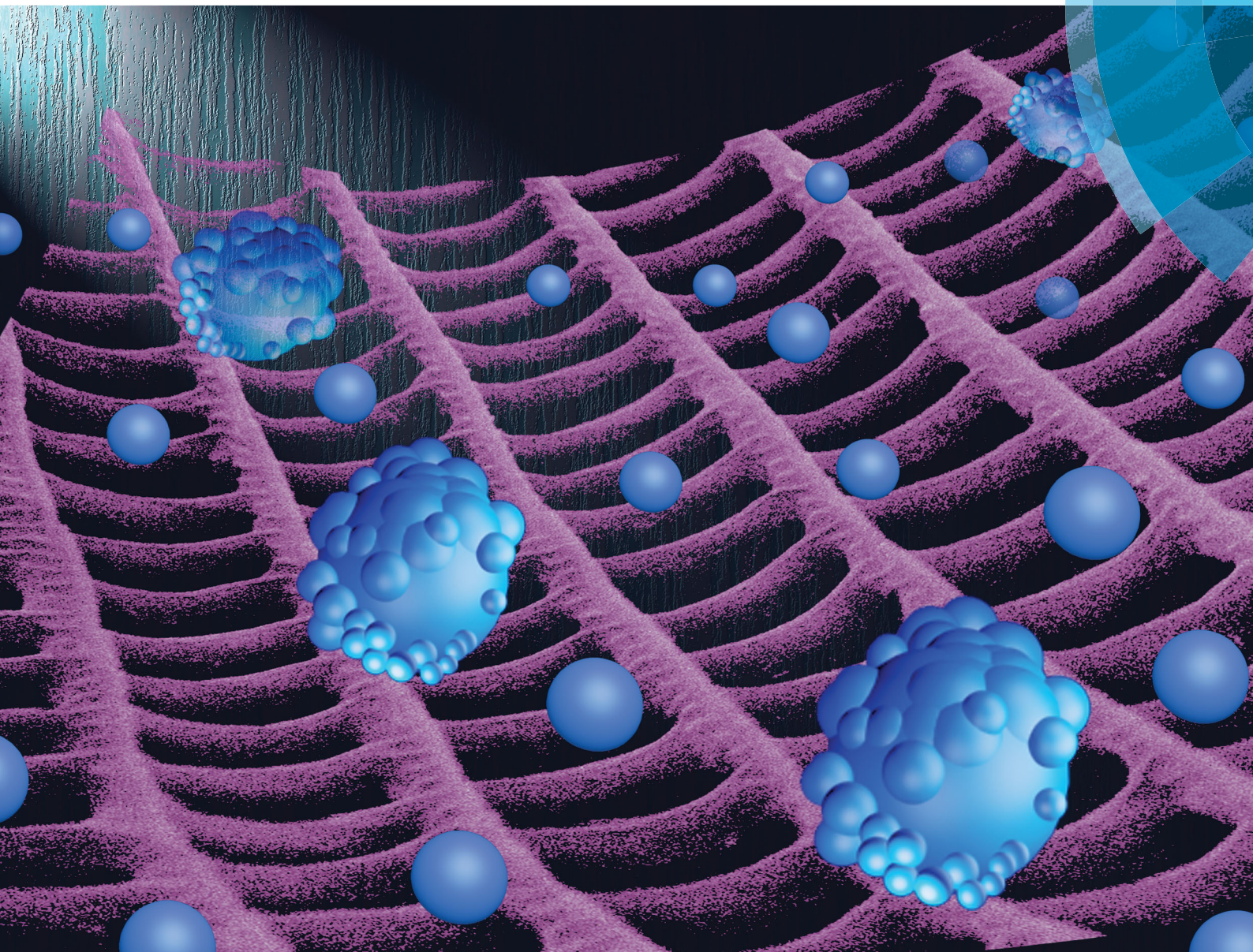
**COMMUNICATION**
Nam-Joon Cho *et al.*
A flexible, ultra-sensitive chemical sensor with 3D biomimetic templating
for diabetes-related acetone detection

## COMMUNICATION

Check for updates

# A flexible, ultra-sensitive chemical sensor with 3D biomimetic templating for diabetes-related acetone detection†

Lili Wang,[ab] Joshua A. Jackman,[a] Jae Hyeon Park,[a] Ee-Lin Tan[a] and
Nam-Joon Cho (ID) *[ac]

The structural features of biological organisms have evolved through natural selection to provide highly tailored functions, inspiring numerous biomimetic and biological design strategies. A wide scope of untapped potential lies in harnessing the nanoscale architectural properties of natural biological materials to develop high-performance sensors. Herein, we report the development of an ultrasensitive chemical sensor that is based on the three-dimensional (3D) biomimetic templating of a structurally hierarchical butterfly wing. In conjunction with graphene sheet coating strategies, the porous 3D architecture enables highly selective detection of diabetes-related volatile organic compounds (VOCs), including a rapid response time (≤1 s), a low limit of detection (20 ppb), and superior mechanical properties. Taken together, the findings in this work demonstrate the promise of incorporating natural biological materials into high-performance sensors, with excellent potential for wearable and flexible sensors.

## Introduction

In nature, flora and fauna possess robust hierarchical structures capable of specialized functions, which have become highly tailored through millions of years of evolution and beyond.[1,2] In particular, structure-driven properties serve important functions in nature and have inspired numerous technological innovations.[3] Indeed, many artificial and biomimetic materials have been developed to mimic the structure and performance of natural materials.[4–6] Although much progress has been achieved, key challenges remain with respect to limitations in accurately recreating or mimicking natural materials.[7,8] Therefore, feasible strategies to effectively combine or adopt natural

micro/nanostructures into functionalized material systems are highly desired.

The Knight butterfly (*Lebadea martha parkeri*) functions as a complex biological actuator that has exceptional microstructures,[9] self-cleaning,[10] structural color,[11] and sensory receptors.[12] Because of these fascinating and alluring physical and chemical properties, the butterfly wing is one of the most promising materials for applications in optical, electronic, energy and chemical sensing.[13,14] In the past few decades, numerous studies have investigated the integration of butterfly wings in optical sensors.[15] In particular, the photonic structures of butterfly wings have been identified to exhibit different optical responses to different types of vapors (such as water, methanol, ethanol, and isomers of dichloroethylene) depending on the wing's coloring and patterning.[12,16] Most of the relevant studies have focused primarily on the physical structures and properties of butterfly wings, but the influence of their intrinsic chemical composition, unique biological functions, and topographical features on sensing functions remain to be explored.

The Knight butterfly wing is a natural polysaccharide polymer, which exhibits beneficial features such as facile chemical functionalization, remarkable mechanical properties, and *in situ* tailoring of chemical composition. Chitosan is a type of linear polysaccharide obtained from the *N*-deacetylation of natural chitin which can be extracted from butterfly wings.[17–19] In particular, chitosan has superb biological characteristics (such as water solubility, biodegradability, renewability, antimicrobial activity, biocompatibility, and adsorption properties) beyond the capabilities of natural chitin.[20–22] Thus, it has received much attention in the fields of bioelectronics, optics, catalysis, food engineering, energy, medicine, and sensing.[23–25] In addition, the chemical reactivity of the free amine groups present along the polysaccharide chain is appropriate in grafting functional materials to form "smart" biocomposites. Several examples of functional chitosan biocomposites that have been developed with chemical modifications (carbon material-coated chitosan, polymer-coated chitosan, and metal oxide-coated chitosan) have been reported.[26–29] Chitosan-based biocomposites are expected to exhibit superior

*[a] School of Materials Science and Engineering, Nanyang Technological University, 50 Nanyang Avenue, 639798 Singapore, Singapore. E-mail: njcho@ntu.edu.sg*

*[b] State Key Laboratory on Integrated Optoelectronics, College of Electronic Science and Engineering, Jilin University, Changchun 130012, P. R. China*

*[c] School of Chemical and Biomedical Engineering, Nanyang Technological University, 62 Nanyang Drive, 637459 Singapore, Singapore*

† Electronic supplementary information (ESI) available. See DOI: 10.1039/c7tb00787f

This journal is © The Royal Society of Chemistry 2017

*J. Mater. Chem. B*, 2017, **5**, 4019–4024 | 4019

mechanical strength, good biocompatibility/biodegradability, remarkable electronic properties and promising synergistic properties that greatly enhance their potential suitability for biological applications such as disease diagnosis,[30] biomarker detection,[31] and drug-delivery.[32] Recently, wearable biosensors composed of ultrathin single-walled carbon nanotubes and chitosan have demonstrated enhanced performance for *in situ* perspiration analysis.[33] Looking forward, the incorporation of this sophisticated hierarchical 3D architecture platform derived from a natural biomaterial together with its biologically inspired functions has shown unprecedented results for sensor applications with respect to performance and sensitivity. However, further improvements in the fabrication process are required to minimize the use of cumbersome methods and to develop ultra-sensitive chemical sensing applications.

Herein, we report a streamlined strategy to design a multifunctional biomaterial by templating the unique surface topography of natural butterfly wings and adding functional features of graphene. The alchemized biomaterial is able to retain its native hierarchical microstructure and is malleable to compositional customization and exhibits unparalleled mechanical properties. In this study, the material was integrated into a chemical sensor to test its capability in detecting diabetes-related acetone vapors. We demonstrate excellent sensing performance that is uncompromised even when challenged with significant bending, making it promising for portable, wearable or even implantable sensors.

## Results and discussion

The microstructure of Knight butterfly wings was employed as a 3D template in order to take advantage of natural periodic patterns, which can deliver specific functions more effectively than products of artificial mimicry (Fig. 1a and b). Because a typical butterfly wing is composed of chitin ($>83\%$),[34] which is a long-chained polymer of $N$-acetylglucosamine (Fig. 1c), compositional alterations in its native state were necessary to facilitate the templating process. Hence, a series of chemical

treatments were introduced to affix functional sensing capabilities to biomaterials (detailed fabrication steps available in the Methods section and Fig. S1a, ESI†).[35] First, chitin extraction from the Knight butterfly wings consists of demineralization, deproteinization, decoloration, and serial washing to remove the pigments, proteins and other mineral constituents from the raw material (Fig. S2a, ESI†). Next, the butterfly wings were alkalized to transform chitin (CT) into chitosan (CS), which is achieved by substituting a number of amino groups into its chemical makeup (Fig. 1c and Fig. S2b, ESI†). The transformation efficiency of this treatment was evaluated by XRD analysis, identifying two distinct diffraction peaks at $2\theta = 9.93°$ and $19.97°$, which have been consistently observed for CT identification (Fig. S2c, ESI†).[36]

FESEM images of the butterfly wing revealed arrays of vertically aligned scale-like skeleton structures (Fig. 1d). A close-up view of an individual scale unveiled a quasi-"honeycomb" architecture consisting of rectangular cells as seen in Fig. 1e, and the native architecture was retained even after the deacetylation treatment to obtain CS as shown in Fig. 1f. By comparison, separately prepared biomimetic CS (synthesis of biomimetic chitosan referenced in the Methods section, ESI†) was unable to accurately mimic the microstructure although chemically identical. Also, as a result of the transformation process, the characteristic hydrophobicity of CT was no longer observed as analysed by the water droplet contact angle measurement, further supporting the successful transformation into CS across the biomaterial surface (insets of Fig. 1e and f).

Owing to its detailed structure, the extracted CS demonstrated excellent flexibility and durability, and was able to resist breakage or fracture when bent or stretched (Fig. S3, ESI†).

To enhance the versatility of materials in applications, multiple components are often integrated into biocomposites to seek synergistic advantages from the collective set of individual physicochemical properties.[6] In the field of sensor applications, many biocomposites have been shown to outperform singular material compositions.[37] Similarly, the same considerations are made here for synthesizing a biocomposite using the naturally extracted CS to maximize its potential application. Fig. 2a shows a simplified schematic route for synthesizing a 3D-structured CS and reduced graphene oxide (3D CS@rGO) biocomposite. Initially, graphene oxide (GO) was introduced into the CS biotemplate, which would weakly interact through hydrogen bonding between the amino groups ($-NH_2$) of CS and the carboxyl groups ($-COOH$) of GO (Fig. 2b).[28,38–40] The relatively unstable CS@GO is then reinforced using simple reduction chemistry to obtain a reduced form of the biocomposite, otherwise denoted as CS@rGO. Fig. S4a (ESI†) shows a C–N stretching bond in the CS@rGO, which is further evidence of rGO attached to the surface of CS. Throughout the process the quasi-"honeycomb" architecture was well-preserved and a proportion of the active sites ($-NH_2$) remained within the biocomposite (Fig. 2c and Fig. S4a, ESI†), which are reserved for sensor-specific functionalities (*e.g.*, recognition, selective adsorption, and sensing).[6,41] Furthermore, the CS@rGO biocomposite exhibited excellent electrical conductivity far superior to the CS@GO biocomposite
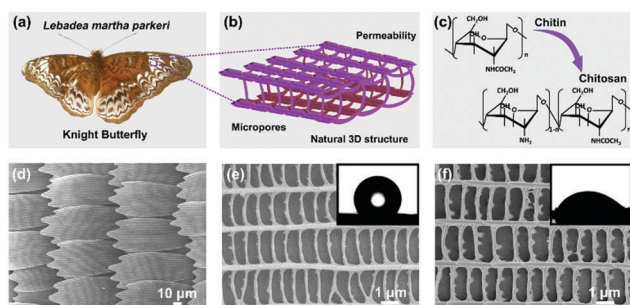


Fig. 1 Structural characterization of the Knight (*Lebadea martha parkeri*) butterfly wing. (a) Anatomical image of the Knight butterfly. (b) A schematic illustration of the microstructure of a Knight butterfly wing segment with a characteristic quasi-"honeycomb" structure. (c) Chemical transformation of chitin to chitosan characterized by its molecular structure. FESEM images reveal the honeycomb structures of (d and e) chitin and (f) chitosan, with inset images demonstrating the corresponding contact angle measurement results.

4020 | *J. Mater. Chem. B*, 2017, 5, 4019–4024

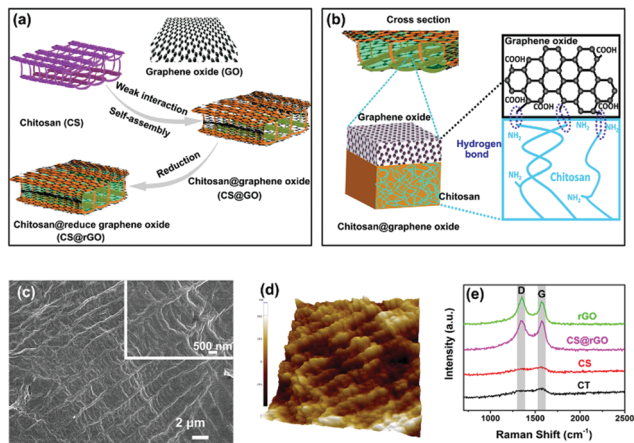This journal is © The Royal Society of Chemistry 2017

Fig. 2 Design, synthesis and characterization of a chitosan/reduced graphene oxide (CS@rGO) biocomposite. (a and b) Schematic illustration of the conjugation of materials based on the self-assembly of CS on graphene oxide (GO) and subsequent reduction to obtain rGO. (c) Low-magnification FESEM image of CS@rGO, and a high-magnification FESEM image in the inset. (d) Topographical features characterized by AFM analysis to show the surface roughness of the final CS@rGO. (e) Raman spectra of CT, CS, CS@rGO, and rGO samples.
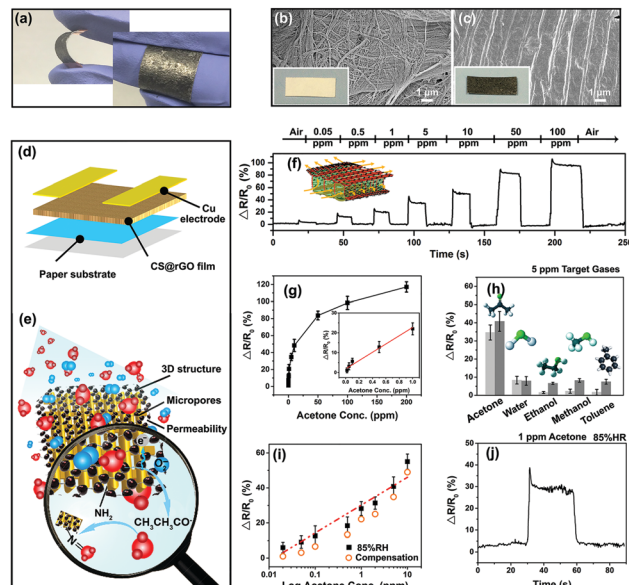


Fig. 3 Design, sensing principle and performance of a flexible sensor based on CS@rGO biocomposites. (a) Flexibility demonstration of the fully assembled sensor unit. The FESEM images and optical images (inset) of the cellulose paper with (b) and without (c) CS@rGO biocomposites. (d) Compositional layout of a single sensor unit, consisting of a CS@rGO biocomposite layer, two copper electrodes, and cellulose paper. (e) Measurement principle of the acetone vapor sensor using CS@rGO biocomposites. (f) Response and recovery curves recorded by the CS@rGO sensor to increasing concentration of acetone vapor from 50 ppb to 100 ppm (measurements taken at room temperature). (g) Sensitivity of the sensor as a function of acetone concentration at room temperature. (h) Response values to different types of vapor molecules introduced at a concentration of 5 ppm – sensor performance evaluated in atmospheric air (light gray) and simulated-exhaled breath (dark gray). (i) Overestimation of acetone vapors (black) compensated by built-in humidity compensation values to accurately adjust measurements (orange). (j) Single cycle of response/recovery recorded by the 3D CS@rGO sensor to 1 ppm acetone in simulated-exhaled breath (85% RH). All error bars display standard deviation for triplicate measurements ($N$ = 3).

and CS-based biocomposites conventionally used for nano-reactors (Fig. S4b, ESI†).

The self-assembly of GO onto the surface of the quasi-"honeycomb" CS was visually distinguishable as shown in the FESEM image in Fig. 2c and Fig. S4c (ESI†). The topographical features of the butterfly wing were intact, but the interspatial voids that were seen between the meshed ridges were completely covered. The new fillers are assumed to be the composite product of rGO and CS and show a distinct texture (Fig. S4d and inset, ESI†), especially in comparison to the CT@rGO biocomposite (Fig. S5, ESI†). In particular, while a relatively flat and featureless surface is observed between the ridges of CT (Fig. S5b–d, ESI†) a contrasting nanoscaled roughness could be easily spotted for the CS@rGO biocomposite (Fig. 2d). Additionally, the Raman spectra of the synthesized CS@rGO presented two distinct peaks at 1329 and 1589 cm$^{-1}$, each one corresponding to D and G bands, respectively. Indeed, the D/G intensity ($I_D/I_G$) value was comparable to that of rGO while clearly different from CS, which further confirmed the successful deposition of rGO on CS (Fig. 2e).

In Fig. 3a, the remarkable mechanical features are demonstrated in consideration of its potential application in wearable electronic devices. This was achieved by using a mechanically flexible cellulose paper as a substrate, and it is also biodegradable and biocompatible (Fig. S6a, ESI†). The CS@rGO biocomposite is deposited on the cellulose paper by suction filtration, and FESEM images confirm distinct features of CS@rGO deposited on the cellulose paper (Fig. 3b and c). Fig. 3d illustrates the assembly of a flexible sensor unit, which consists of a functional sensor layer, two copper electrodes, and a cellulose paper layer to support the device. The fully assembled sensor was then wired to a home-made gas chamber equipped with electrical feedthroughs (Fig. S6b, ESI†).

The 3D CS@rGO biocomposite was chosen as the core unit for the sensor to satisfy two fundamental design aspects (Fig. 3e). First, utilizing CS as the main material for the sensor unit is critical. CS possesses a number of –NH$_2$ groups that remain exposed even after coating with rGO (Fig. S4a, ESI†), which specifically interact with the carbonyl groups of acetone, contributing to the high specificity of the sensor (Fig. S7a, ESI†).[42] Second, the biocomposite layer is derived from a unique and natural 3D hierarchical structure which is coincidentally advantageous for its function (Fig. 3e and Fig. S7b and f, ESI†). Indeed, the naturally porous surface effectively avoids "dead volume", thus accelerating the diffusion of gas molecules. The 3D honeycomb structure offers a large surface area and effectively increases the utilization ratio of the sensing material. In comparison to the bulk material (Fig. S7c and g, ESI†), a non-structured film (Fig. S7d and g, ESI†) and pure rGO (Fig. S7e and i, ESI†), the natural, highly porous structure enhances the sensing responsivity to the adsorption of acetone molecules, thereby having greater surface area available for detection and greater accessibility for target gases.[43–45]

This journal is © The Royal Society of Chemistry 2017

J. Mater. Chem. B, 2017, 5, 4019–4024 | 4021

Acetone, a volatile organic compound (VOC), has been previously identified as an important biomarker for diabetes that can be detected from exhaled breath.[46] In particular, approximately 1800 ppb is detected from diabetic patients, while only 300–900 ppb are recorded for a non-diabetic person.[47] In order to design a proof-of-concept sensor device for diabetes using our chemisensor, performance evaluation was first conducted in a closed-chamber setup. The sensor sensitivity, which is calculated based on the relative change in conductance ($\Delta R/R_0$, where $R_0$ is initial resistance and $\Delta R = R - R_0$, see the Methods section, ESI†), was recorded with injections of different acetone vapor concentrations in a home-made gas chamber (Fig. S6b, ESI†). The sensitivity of the 3D CS@rGO sensor ranged from 3.5% to 96.7% across the range of acetone concentrations from 0.05 to 100 ppm (Fig. 3f). More importantly, the sensor demonstrated a rapid response and recovery characteristics (Fig. S8, ESI†) and excellent stability (Fig. S9, ESI†) regardless of vapor concentration, and an extremely low limit of detection (Fig. 3g) was achieved, surpassing performance records of other similarly designed acetone vapor sensors (Table S1, ESI†).

Next, the selectivity of the sensor was tested with various gases including acetone, water, ethanol, methanol, and toluene, respectively. Sensitivity to acetone was exceptionally high compared to the other gases as seen in Fig. 3h, and the specificity was similarly observed in simulated exhaled breath (85% RH, see details in the Methods section, ESI†). Complementary experiments indicated that humidity reflected the effect of increased acetone sensing activities (Fig. S10a and b, ESI†). To calibrate the measurement sensitivity, real-time compensation on the basis of humidity variations was incorporated. Fig. 3i shows that, in simulated exhaled breath (85% RH), the sensitivity of the uncompensated sensor can cause overestimation of the actual concentration of acetone vapors; however, the humidity compensation allows for accurate and consistent evaluation. On the other hand, consistency in the sensor response rate was noted to be unaffected by humidity variation (Fig. 3j and Fig. S10 and Movie S1, ESI†), which, to our best knowledge, is the fastest among reported vapor sensors. From the overall performance evaluation, the 3D CS@rGO sensor demonstrated high accuracy, high sensitivity, and a rapid response rate, offering significant advantages and great potential for physiological monitoring applications (Table S2, ESI†).

Considering that the chemical sensor would be intended for use in wearable electronics, the device was designed to be extremely flexible, light, soft, robust, and biocompatible in order to endure the stress of daily activities.[37,48–50] Hence, the mechanical durability and the relevant performance were tested by measuring the change in resistance against mechanical stress as indicated by bending angles from 0° to 40° (Fig. 4a–e). Negligible differences in resistance values were observed despite the applied stress (Fig. 4a), and the sensitivity of the sensor was not hindered when tested with 0.5 ppm acetone vapors (85% RH), recording approximately 16.7 ± 0.8% responses (Fig. 4b–e and Fig. S11, ESI†).

Furthermore, the sensing response of the device to a sudden change in the bending angle was also tested (Fig. 4f), with approximately a 20–40% change in the sensor sensitivity. The
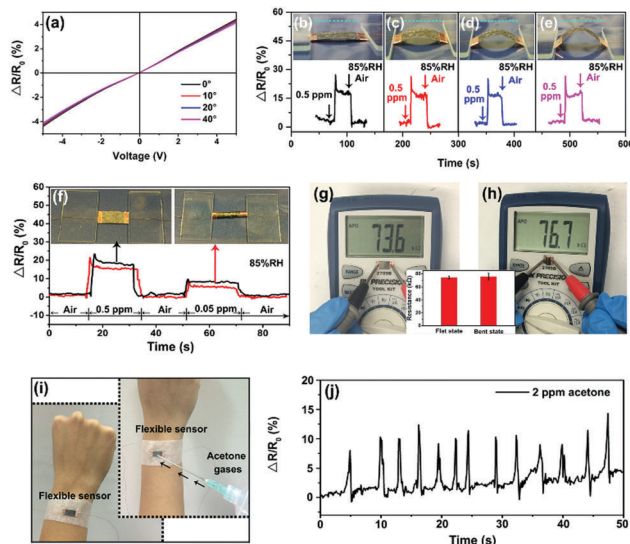


Fig. 4 Sensor performance evaluation under mechanical stress. (a) $I$–$V$ curves of the 3D CS@rGO sensor responding to various bending angles. (b–e) Transient plots of the measurement response curves to 0.5 ppm of acetone (85% RH) when positioned at various bending angles. (f) Comparison of the sensing performance of the 3D CS@rGO sensor under flat and bent states. (g and h) Resistance values of the 3D CS@rGO sensor before and after bending. The inset histogram shows mean resistance values from triplicate measurements under each defined condition. (i) Photograph of a proof-of-concept wearable sensor and illustration of the performance evaluation method. (j) Real-time sensor response to a pulsated ejection of simulated diabetic breath containing 2 ppm of acetone vapor (85% RH) flown directly over the sensor.

decreases in sensitivity of the device in the suddenly bent state are expected, which could be due to the effects of common tear and wear as visualized in FESEM images (Fig. S12, ESI†). Nevertheless, no significant deterioration in the sensor surface was observed besides minor cracks and hinges. Direct measurement by a multimeter revealed an increase in resistance caused by bending (Fig. 4g and h), which further increased with repetitive bending (Fig. S13, ESI†). Despite some loss in electrical conductivity, the sensor still remained functionally intact with high sensitivity and quick responsivity in detection of different concentrations of acetone vapors (Fig. S14, ESI†).

Based on these excellent mechanical properties, a proof-of-concept flexible sensor was created to be designed as a wrist band (Fig. 4i). Inherently, the flexible design would require the sensor to be fully exposed to air as it emulates a convenient diabetes monitor which would collect data from exhalants. The responsiveness of the sensor to simulated exhalants is demonstrated by the plot in Fig. 4j. Under motion conditions, acetone vapor levels on the wrist follow similar trends that are calculated to be approximately 12.1 to 2 ppm acetone vapor, but there is a noticeable decrease in the sensitivity compared with measurements obtained under static conditions (Fig. 4j and Fig. S15, ESI†). The difference is due to the dilution effect that causes a decrease in acetone concentration as the relatively small amount of acetone vapor was captured on the surface of the sensors. The limit of detection of the sensor, however, was estimated to be 0.02 ppm with a sensitivity of 1.2%, which was

still significantly low especially in comparison to clinical standards.[47] As a result, the sensor exemplifies ultra-high sensitivity and selectivity, and features real-time monitoring capabilities that make it a highly desirable platform for portable and wearable sensor applications.

## Conclusions

In summary, we demonstrate the full fabrication process to create a natural, flexible, and high performance chemiresistor sensor. We were able to fabricate an ultrasensitive sensor in a streamlined fashion by effectively utilizing a natural architecture and combining it with highly functional materials. The superiority of this material design approach was demonstrated by the ultra-high sensitivity, rapid response time ($\leq 1$ s), and low limit of detection (20 ppb) of the resulting biocomposite material in comparison to other structured materials, and its applicability is further seen in a chemical sensor design for real-time diabetes monitoring. With the effective adaptation of the material's core functions and physicochemical properties, we were able to develop a flexible, biocompatible, and high performance biosensor that show promising potential for the future of wearable and implantable sensor applications.

## Acknowledgements

## Notes and references

1  J. J. Gu, W. Zhang, H. L. Su, T. X. Fan, S. M. Zhu, Q. L. Liu and D. Zhang, *Adv. Mater.*, 2015, **27**, 464–478.

2  P. Vukusic, B. Hallam and J. Noyes, *Science*, 2007, **315**, 348.

3  D. Van Opdenbosch, G. Fritz-Popovski, W. Wagermaier, O. Paris and C. Zollfrank, *Adv. Mater.*, 2016, **28**, 5235–5240.

4  H. Lee, B. P. Lee and P. B. Messersmith, *Nature*, 2007, **448**, 338–U334.

5  C. Sanchez, H. Arribart and M. M. G. Guille, *Nat. Mater.*, 2005, **4**, 277–288.

6  L. Wang, W. Ng, J. A. Jackman and N.-J. Cho, *Adv. Funct. Mater.*, 2016, **26**, 2097–2103.

7  H. W. Chen, P. F. Zhang, L. W. Zhang, H. L. L. Iu, Y. Jiang, D. Y. Zhang, Z. W. Han and L. Jiang, *Nature*, 2016, **532**, 85.

8  G. T. Zan and Q. S. Wu, *Adv. Mater.*, 2016, **28**, 2099–2147.

9  C. C. Liu, J. Ju, Y. M. Zheng and L. Jiang, *ACS Nano*, 2014, **8**, 1321–1329.

10  Y. M. Zheng, X. F. Gao and L. Jiang, *Soft Matter*, 2007, **3**, 178–182.

11  A. Singer, L. Boucheron, S. H. Dietze, K. E. Jensen, D. Vine, I. McNulty, E. R. Dufresne, R. O. Prum, S. G. J. Mochrie and O. G. Shpyrko, *Sci. Adv.*, 2016, **2**, 6.

12  R. A. Potyrailo, R. K. Bonam, J. G. Hartley, T. A. Starkey, P. Vukusic, M. Vasudev, T. Bunning, R. R. Naik, Z. X. Tang, M. A. Palacios, M. Larsen, L. A. Le Tarte, J. C. Grande, S. Zhong and T. Deng, *Nat. Commun.*, 2015, **6**, 12.

13  F. Y. Zhang, Q. C. Shen, X. D. Shi, S. P. Li, W. L. Wang, Z. Luo, G. F. He, P. Zhang, P. Tao, C. Y. Song, W. Zhang, D. Zhang, T. Deng and W. Shang, *Adv. Mater.*, 2015, **27**, 1077–1082.

14  S. Lou, X. M. Guo, T. X. Fan and D. Zhang, *Energy Environ. Sci.*, 2012, **5**, 9195–9216.

15  R. A. Potyrailo, H. Ghiradella, A. Vertiatchikh, K. Dovidenko, J. R. Cournoyer and E. Olson, *Nat. Photonics*, 2007, **1**, 123–128.

16  R. A. Potyrailo, T. A. Starkey, P. Vukusic, H. Ghiradella, M. Vasudev, T. Bunning, R. R. Naik, Z. X. Tang, M. Larsen, T. Deng, S. Zhong, M. Palacios, J. C. Grande, G. Zorn, G. Goddard and S. Zalubovsky, *Proc. Natl. Acad. Sci. U. S. A.*, 2013, **110**, 15567–15572.

17  N. Yan and X. Chen, *Nature*, 2015, **524**, 155–157.

18  W. Suginta, P. Khunkaewla and A. Schulte, *Chem. Rev.*, 2013, **113**, 5458–5479.

19  S. Ladet, L. David and A. Domard, *Nature*, 2008, **452**, 76–U76.

20  T. J. Mooibroek, J. M. Casas-Solvas, R. L. Harniman, C. Renney, T. S. Carter, M. P. Crump and A. P. Davis, *Nat. Chem.*, 2016, **8**, 69–74.

21  J. X. Jian, Q. Liu, Z. J. Li, F. Wang, X. B. Li, C. B. Li, B. Liu, Q. Y. Meng, B. Chen, K. Feng, C. H. Tung and L. Z. Wu, *Nat. Commun.*, 2013, **4**, 9.

22  A. Anitha, S. Sowmya, P. T. S. Kumar, S. Deepthi, K. P. Chennazhi, H. Ehrlich, M. Tsurkan and R. Jayakumar, *Prog. Polym. Sci.*, 2014, **39**, 1644–1667.

23  M. Yalpani, L. D. Hall, M. A. Tung and D. E. Brooks, *Nature*, 1983, **302**, 812–814.

24  C. Zhong, Y. X. Deng, A. F. Roudsari, A. Kapetanovic, M. P. Anantram and M. Rolandi, *Nat. Commun.*, 2011, **2**, 5.

25  D. Peer, J. M. Karp, S. Hong, O. C. FaroKhzad, R. Margalit and R. Langer, *Nat. Nanotechnol.*, 2007, **2**, 751–760.

26  M. Semsarilar and S. Perrier, *Nat. Chem.*, 2010, **2**, 811–820.

27  E. Miyako, T. Sugino, T. Okazaki, A. Bianco, M. Yudasaka and S. Iijima, *ACS Nano*, 2013, **7**, 8736–8742.

28  Q. Q. Yang, S. M. Zhu, W. H. Peng, C. Yin, W. L. Wang, J. J. Gu, W. Zhang, J. Ma, T. Deng, C. L. Feng and D. Zhang, *ACS Nano*, 2013, **7**, 4911–4918.

29  D. D. Xu, H. A. Yu, Q. Xu, G. H. Xu and K. X. Wang, *ACS Appl. Mater. Interfaces*, 2015, **7**, 8750–8756.

30  T. Gordonov, E. Kim, Y. Cheng, H. Ben-Yoav, R. Ghodssi, G. Rubloff, J. J. Yin, G. F. Payne and W. E. Bentley, *Nat. Nanotechnol.*, 2014, **9**, 605–610.

31  M. G. Zhang and W. Gorski, *J. Am. Chem. Soc.*, 2005, **127**, 2058–2059.

32  M. Cuna, M. Alonso-Sande, G. Remunan-Lopez, J. P. Pivel, J. L. Alonso-Lebrero and M. J. Alonso, *J. Nanosci. Nanotechnol.*, 2006, **6**, 2887–2895.

This journal is © The Royal Society of Chemistry 2017

*J. Mater. Chem. B*, 2017, **5**, 4019–4024 | 4023

33 W. Gao, S. Emaminejad, H. Y. Y. Nyein, S. Challa, K. V. Chen, A. Peck, H. M. Fahad, H. Ota, H. Shiraki, D. Kiriya, D. H. Lien, G. A. Brooks, R. W. Davis and A. Javey, *Nature*, 2016, **529**, 509–514.

34 W. Zhang, J. J. Gu, Q. L. Liu, H. L. Su, T. X. Fan and D. Zhang, *Phys. Chem. Chem. Phys.*, 2014, **16**, 19767–19780.

35 S. Kaur and G. S. Dhillon, *Crit. Rev. Biotechnol.*, 2015, **35**, 44–61.

36 N. Sayari, A. Sila, B. E. Abdelmalek, R. Ben Abdallah, S. Ellouz-Chaabouni, A. Bougatef and R. Balti, *Int. J. Biol. Macromol.*, 2016, **87**, 163–171.

37 L. Wang, J. A. Jackman, W. B. Ng and N.-J. Cho, *Adv. Funct. Mater.*, 2016, **26**, 8623–8630.

38 J. Balapanuru, J.-X. Yang, S. Xiao, Q. Bao, M. Jahan, L. Polavarapu, J. Wei, Q. H. Xu and K. P. Loh, *Angew. Chem.*, 2010, **122**, 6699–6703.

39 Y. Wang, L. Polavarapu and L. M. Liz-Marzan, *ACS Appl. Mater. Interfaces*, 2014, **6**, 21798–21805.

40 Z. Guan, L. Polavarapu and Q.-H. Xu, *Langmuir*, 2010, **26**, 18020–18023.

41 P. T. Yin, S. Shah, M. Chhowalla and K. B. Lee, *Chem. Rev.*, 2015, **115**, 2483–2531.

42 Y. Kurita and A. Isogai, *Int. J. Biol. Macromol.*, 2010, **47**, 184–189.

43 W. T. Koo, S. J. Choi, S. J. Kim, J. S. Jang, H. L. Tuller and I. D. Kim, *J. Am. Chem. Soc.*, 2016, **138**, 13431–13437.

44 L. L. Wang, T. Fei, Z. Lou and T. Zhang, *ACS Appl. Mater. Interfaces*, 2011, **3**, 4689–4694.

45 L. L. Wang, H. M. Dou, Z. Lou and T. Zhang, *Nanoscale*, 2013, **5**, 2686–2691.

46 J. Shin, S.-J. Choi, I. Lee, D.-Y. Youn, C. O. Park, J.-H. Lee, H. L. Tuller and I.-D. Kim, *Adv. Funct. Mater.*, 2013, **23**, 2357–2367.

47 J. S. Jang, S. J. Kim, S. J. Choi, N. H. Kim, M. Hakim, A. Rothschild and I. D. Kim, *Nanoscale*, 2015, **7**, 16417–16426.

48 T. Q. Trung and N. E. Lee, *Adv. Mater.*, 2016, **28**, 4338–4372.

49 M. C. McAlpine, H. Ahmad, D. W. Wang and J. R. Heath, *Nat. Mater.*, 2007, **6**, 379–384.

50 Z. Lou, S. Chen, L. L. Wang, K. Jiang and G. Z. Shen, *Nano Energy*, 2016, **23**, 7–14.